

Northumbria Research Link

Citation: Ren, Xiaohe, Sun, Mengxuan, Gan, Ziwei, Li, Zhijie, Cao, Baobao, Shen, Wenzhong and Fu, Yong Qing (2022) Hierarchically nanostructured Zn_{0.76}Co_{0.24}S@Co(OH)₂ for high-performance hybrid supercapacitor. Journal of Colloid and Interface Science, 618. pp. 88-97. ISSN 0021-9797

Published by: Elsevier

URL: <https://doi.org/10.1016/j.jcis.2022.03.069>
<<https://doi.org/10.1016/j.jcis.2022.03.069>>

This version was downloaded from Northumbria Research Link:
<https://nrl.northumbria.ac.uk/id/eprint/48807/>

Northumbria University has developed Northumbria Research Link (NRL) to enable users to access the University's research output. Copyright © and moral rights for items on NRL are retained by the individual author(s) and/or other copyright owners. Single copies of full items can be reproduced, displayed or performed, and given to third parties in any format or medium for personal research or study, educational, or not-for-profit purposes without prior permission or charge, provided the authors, title and full bibliographic details are given, as well as a hyperlink and/or URL to the original metadata page. The content must not be changed in any way. Full items must not be sold commercially in any format or medium without formal permission of the copyright holder. The full policy is available online: <http://nrl.northumbria.ac.uk/policies.html>

This document may differ from the final, published version of the research and has been made available online in accordance with publisher policies. To read and/or cite from the published version of the research, please visit the publisher's website (a subscription may be required.)

Hierarchically nanostructured $\text{Zn}_{0.76}\text{C}_{0.24}\text{S}@\text{Co}(\text{OH})_2$ for high- performance hybrid supercapacitor

Xiaohe Ren^a, Mengxuan Sun^a, Ziwei Gan^a, Zhijie Li^{a,*}, Baobao Cao^b, Wenzhong
Shen^c, YongQing Fu^{d,*}

^a School of Physics, University of Electronic Science and Technology of China,
Chengdu, 6111731, P. R. China

^b Key Laboratory of Advanced Technologies of Materials, Ministry of Education,
Southwest Jiaotong University, Chengdu 610031, PR China

^c State Key Laboratory of Coal Conversion, Institute of Coal Chemistry, Chinese
Academy of Science, Taiyuan, 030001, P. R. China

^d Faculty of Engineering and Environment, Northumbria University, Newcastle Upon
Tyne, NE1 8ST, UK

Zhijie Li (**Corresponding Author**): ORCID: 0000-0001-9870-9939;

*E-mail: zhijieli@uestc.edu.cn; TEL: +86 02883202160

Yongqing (Richard) Fu (**Corresponding Author**): ORCID: 0000-0001-9797-4036;

*E-mail: Richard.fu@northumbria.ac.uk; TEL: +44 (0)191 2274662

Abstract

It is a great challenge to achieve both high specific capacity and high energy density of supercapacitors by designing and constructing hybrid electrode materials through a simple but effective process. In this paper, we proposed a hierarchically nanostructured hybrid material combining $\text{Zn}_{0.76}\text{Co}_{0.24}\text{S}$ (ZCS) nanoparticles and $\text{Co}(\text{OH})_2$ (CH) nanosheets using a two-step hydrothermal synthesis strategy. Synergistic effects between ZCS nanoparticles and CH nanosheets result in efficient ion transports during the charge-discharge process, thus achieving a good electrochemical performance of the supercapacitor. The synthesized ZCS@CH hybrid exhibits a high specific capacity of 1152.0 C g^{-1} at a current density of 0.5 A g^{-1} in 2 M KOH electrolyte. Its capacity retention rate is maintained at $\sim 70.0\%$ when the current density is changed from 1 A g^{-1} to 10 A g^{-1} . A hybrid supercapacitor (HSC) assembled from ZCS@CH as the cathode and active carbon (AC) as the anode displays a capacitance of 155.7 F g^{-1} at 0.5 A g^{-1} , with a remarkable cycling stability of 91.3% after 12,000 cycles. Meanwhile, this HSC shows a high energy density of 62.5 Wh kg^{-1} at a power density of 425.0 W kg^{-1} , proving that the developed ZCS@CH is a promising electrode material for energy storage applications.

Keywords: Supercapacitor, $\text{Zn}_{0.76}\text{Co}_{0.24}\text{S}$, $\text{Co}(\text{OH})_2$, Hybrid nanostructures, Hydrothermal method

1 Introduction

It has been a great challenge to develop green, environment-friendly, clean and sustainable energy for coping with the global issues of energy shortage and environmental pollution and applying electrical novel energy storage technologies for electric vehicles, portable electronics, and medical devices [1-3]. Currently, supercapacitors (SCs) are considered to be one of the most promising energy storage devices due to their fast charging and discharging rates, long lifetime and relatively high power density [4, 5]. Nevertheless, their low energy densities hinder their practical applications. To solve this issue, various types of supercapacitors have been developed to achieve a high energy density. According to different storage mechanisms of cathodes and anodes, SCs can be classified into a symmetrical type, an asymmetric type and a hybrid type supercapacitor (HSC) [6]. Among them, the HSC is commonly constructed by combining capacitive-type and battery-type electrodes, which can achieve a high specific energy density [6-8].

In recently years, nanomaterials based on transition metal hydroxides, including $\text{Co}(\text{OH})_2$ [9], $\text{Ni}(\text{OH})_2$ [10] and $\text{Cu}(\text{OH})_2$ [11], have been explored as the promising battery-type cathode materials for the HSCs, because they have large spacings among layers and can provide preferably large surface areas and efficient ion transport channels [12]. Among them, $\text{Co}(\text{OH})_2$ has a theoretical capacitance of 3500.0 F g^{-1} [13]. However, its poor conductivity affects its capacity, energy density and cycling stability [14, 15]. To solve these issues, carbon materials with their excellent electrical conductivities have been added into the $\text{Co}(\text{OH})_2$. For examples, an $\text{Co}(\text{OH})_2/\text{AC}$

nanocomposite synthesized using a precipitation method exhibited a high specific capacity of 447.0 C g^{-1} at 1 A g^{-1} [16]. A composite of Co(OH)_2 and GO showed a specific capacitance of 1014.0 F g^{-1} at 1 A g^{-1} [17]. However, these reported capacitance values are still much smaller than the theoretically predicated ones of Co(OH)_2 .

Recently bimetallic sulfide compounds are investigated as the promising battery-type cathode materials, due to their high electrical conductivities and multiple redox reactions [18]. For examples, zinc and cobalt have good coordination abilities. Zinc has a larger atomic radius than cobalt. Zinc cobalt sulfides possess much lower optical band gaps and display a good electrochemical performance [19]. Li et al. reported that $\text{Zn}_{0.76}\text{Co}_{0.24}\text{S}$ nanoparticles synthesized using a two-step hydrothermal method achieved a specific capacitance of 1269.1 F g^{-1} at 0.5 A g^{-1} [20]. Yang et al. used a combined precipitation and ion-exchange method to prepare ZnCoS nanoparticles, which achieved a specific capacitance of 1134.7 F g^{-1} at 1 A g^{-1} [21]. Although zinc cobalt sulfides have shown high electrical conductivities, their specific capacities are still quite low [22].

Hybrid materials integrated with bimetallic sulfides and transition metal hydroxides can achieve a synergistic effect and thus a significantly increased specific capacity. For example, a core-shell structure of $\text{NiCo}_2\text{S}_4@\text{Co(OH)}_2$ showed a high specific capacity of 1054.9 F g^{-1} at 2 mA cm^2 , and an HSC of $\text{NiCo}_2\text{S}_4@\text{Co(OH)}_2//\text{AC}$ maintained 70.0% of its original capacitance value after 5000 cycles [23]. $\text{CoS}_x/\text{Ni-Co}$ double-layered hydroxides [24] synthesized using etching and precipitation approaches showed a specific capacitance of 1562.0 F g^{-1} at 1 A g^{-1} , and the synthesized HSC showed an

energy density of 35.8 Wh kg⁻¹ at 800.0 W kg⁻¹. However, the energy density and cycling stability of these hybrid bimetallic sulfides and transition metal hydroxides are still needed to improve. They were often grown directly on the collectors using a complicated electrochemical deposition method [22, 23, 25]. Therefore, it is urgently required to explore a simple but effective method to synthesize high performance bimetallic sulfides or transition metal hydroxides for the HSC applications.

In this work, we develop a facile two-step hydrothermal method to synthesize a hybrid electrode material of uniformly distributed Zn_{0.76}Co_{0.24}S nanoparticles and Co(OH)₂ nanosheets (ZCS@CH). The designed structure is schematically illustrated in Figure 1. The synergistic effect between nanoparticles and nanosheets is utilized to achieve a high electrochemical performance, which is mainly attributed to the synergistic effects of Zn_{0.76}Co_{0.24}S nanoparticles and highly conductive Co(OH)₂ nanosheets with large specific surface areas and abundant active sites. Due to these reasons, the hybrid ZCS@CH electrode achieves a large specific capacity of 1152.0 C g⁻¹ at 0.5 A g⁻¹ and a good rate capability. In addition, an HSC assembled with ZCS@CH//AC devices achieves a high energy density of 62.5 Wh kg⁻¹ at a power density of 425.0 W kg⁻¹, and displays an excellent cycling stability.

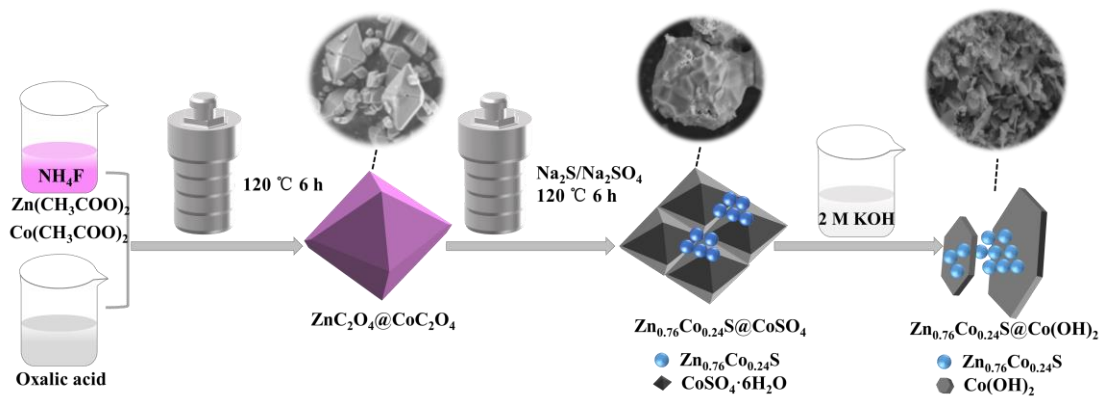


Fig. 1 Schematic illustrations of structure and process of hierarchically nanostructured $\text{Zn}_{0.76}\text{Co}_{0.24}\text{S}@\text{Co}(\text{OH})_2$.

2 Experimental

2.1 synthesis methods

2.1.1 Fabrication of $\text{ZnC}_2\text{O}_4@\text{CoC}_2\text{O}_4$ precursor

$\text{Zn}(\text{CH}_3\text{COO})_2 \cdot 2\text{H}_2\text{O}$ (0.219 g, 1 mmol), $\text{Co}(\text{CH}_3\text{COO})_2 \cdot 4\text{H}_2\text{O}$ (0.498 g, 2 mmol), and NH_4F (0.222 g, 6 mmol) were dissolved in deionized (DI) water (50 ml) and stirred for 10 min at room temperature to obtain a pink solution. Oxalic acid (0.756 g, 6 mmol) was dissolved in DI water (25 ml), added into the above mixed solution, and then stirred continuously for about 5 min. The mixed solution was sealed in a 100 ml Teflon-lined stainless-steel autoclave and kept at 120 °C for 6 h. After cooled down to room temperature, the obtained pink precipitate was washed with DI water and ethanol for several times, and then dried overnight at 60 °C to obtain the precursor of $\text{ZnC}_2\text{O}_4@\text{CoC}_2\text{O}_4$.

2.1.2 Fabrication of $\text{ZCS}@\text{CH}$

$\text{ZnC}_2\text{O}_4@\text{CoC}_2\text{O}_4$ precursor (0.1 g), $\text{Na}_2\text{SO}_4 \cdot 10\text{H}_2\text{O}$ (0.75 g) and $\text{Na}_2\text{S} \cdot 9\text{H}_2\text{O}$ (0.5 g) were mixed inside a 100 ml Teflon-lined stainless-steel autoclave with 75 ml DI water.

The mixture was heated to 120 °C and maintained for 6 h, and then dried at 60°C for 12 h to obtain the black powder of $\text{Zn}_{0.76}\text{Co}_{0.24}\text{S}@\text{CoSO}_4$. In the hydrothermal reaction process, $\text{Na}_2\text{SO}_4 \cdot 10\text{H}_2\text{O}$ and $\text{Na}_2\text{S} \cdot 9\text{H}_2\text{O}$ were used to produce $\text{CoSO}_4 \cdot 6\text{H}_2\text{O}$ and $\text{Zn}_{0.76}\text{Co}_{0.24}\text{S}$, respectively. Then an intermediate material of $\text{Zn}_{0.76}\text{Co}_{0.24}\text{S}@\text{CoSO}_4 \cdot 6\text{H}_2\text{O}$ was produced by the hydrothermal reaction. Finally, the obtained powder of $\text{Zn}_{0.76}\text{Co}_{0.24}\text{S}@\text{CoSO}_4 \cdot 6\text{H}_2\text{O}$ was immersed in a solution of 2 M KOH for overnight, and then cleaned by DI water to obtain the final product of $\text{Zn}_{0.76}\text{Co}_{0.24}\text{S}@\text{Co}(\text{OH})_2$. The procedures are schematically illustrated in Figure 1.

2.1.3 Fabrication of ZCS

For comparison, pure ZCS samples were also synthesized using the same hydrothermal method, but without adding $\text{Na}_2\text{SO}_4 \cdot 10\text{H}_2\text{O}$. The $\text{ZnC}_2\text{O}_4@\text{CoC}_2\text{O}_4$ precursor (0.1 g) and $\text{Na}_2\text{S} \cdot 9\text{H}_2\text{O}$ (1.5 g) were dissolved in DI water (75 ml) and then transferred into a 100 mL autoclave for the hydrothermal process at 120 °C for 6 h. Finally, the precipitate was cleaned using DI water and dried to obtain the ZCS sample. In this process, because there was no $\text{Na}_2\text{SO}_4 \cdot 10\text{H}_2\text{O}$ added, the $\text{CoSO}_4 \cdot 6\text{H}_2\text{O}$ was not produced, thus all the precursors were transformed into $\text{Zn}_{0.76}\text{Co}_{0.24}\text{S}$ sample.

2.3 Characterization methods

Crystalline structures of electrode materials were analyzed using an X-ray diffractometer (XRD, Cu $\text{K}\alpha$, Rigaku D/max-2400). A scanning electron microscope (SEM, Inspect F50) was used to characterize surface morphology of the samples. The microstructures were observed using a transmission electron microscope (TEM, JEM-2200FS, Japan) equipped with an energy-dispersive X-ray spectrometer (EDS). An X-

ray photoelectron spectroscopy (XPS, Al K α radiation, ESCALAB 250Xi) was used to characterize the chemical valence states of the elements. Specific surface areas of the samples were characterized using the Brunauer-Emmett-Teller (BET) technique, and their pore volumes and pore size distributions were obtained using a Barrett-Joyner-Halenda (BJH) method.

2.4 Electrochemical characterization

Electrochemical properties of electrode materials were tested using an electrochemical workstation (CHI660E Chenhua, Shanghai) at room temperature (25 °C) in a 2 M KOH solution. The mixed slurry of the active materials, carbon black and binder of polyvinyl fluoride with a mass ratio of 8:1:1 was coated on a cleaned nickel foam (1×1 cm²) and dried in a vacuum chamber at 50 °C for overnight. The obtained product was used as the working electrodes, which was then combined with the counter electrode of platinum plate and the reference electrode of Hg/HgO to form a three-electrode testing system and test the electrochemical performance. The methods of cyclic voltammetry (CV), galvanostatic charge-discharge (GCD) and electrochemical impedance spectroscopy (EIS) were all performed.

Hybrid supercapacitor (HSC) was fabricated using ZCS@CH as the positive electrode and AC as the negative electrode. The preparation process of AC electrode is the same as that for the working electrode. To achieve the charge balance between positive and negative electrodes in this dual electrode test system, the mass loading of negative material (m_-) was calculated using the following formula [26]:

$$\frac{m_+}{m_-} = \frac{C_- \times \Delta V_-}{C_+ \times \Delta V_+} \quad (1)$$

where m_+ and m_- represent the masses, C_+ and C_- is specific capacities, ΔV_+ and ΔV_- are the potential windows, of both the positive and negative electrodes, respectively.

3 Results and discussion

3.1 Structure and morphology characterization

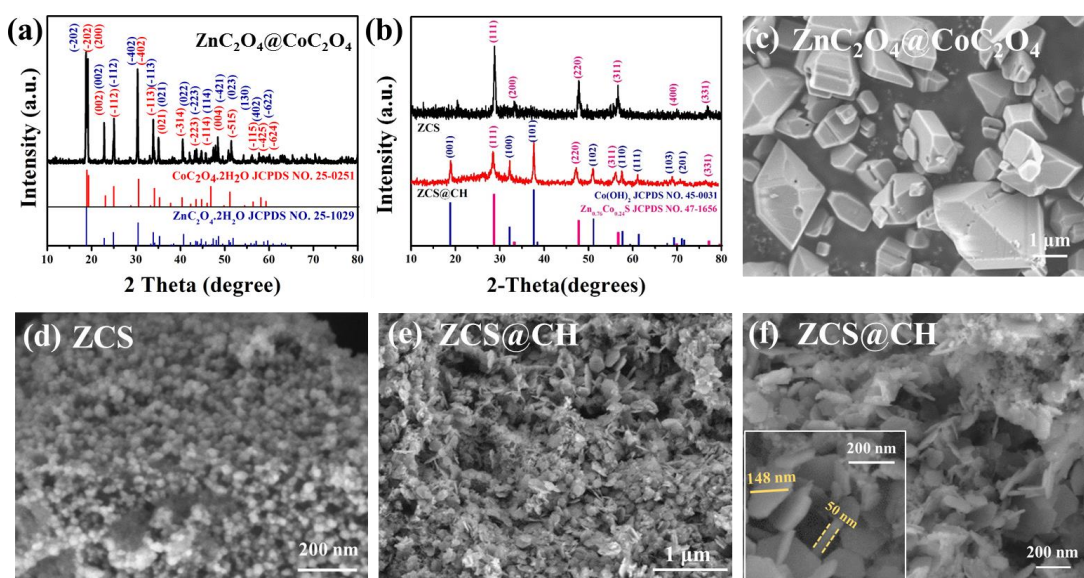


Fig. 2 XRD spectra of (a) precursor of $\text{ZnC}_2\text{O}_4@\text{CoC}_2\text{O}_4$ and (b) pure ZCS and $\text{ZCS}@CH$ samples, SEM images of (c) $\text{ZnC}_2\text{O}_4@\text{CoC}_2\text{O}_4$, (d) ZCS, (e) and (f) $\text{ZCS}@CH$.

Fig. 2a presents an XRD spectrum of the precursor, which shows that the precursor has a good crystallinity and has a mixture of $\text{CoC}_2\text{O}_4 \cdot 2\text{H}_2\text{O}$ and $\text{ZnC}_2\text{O}_4 \cdot 2\text{H}_2\text{O}$. After the hydrothermal reactions using $\text{Na}_2\text{SO}_4 \cdot 10\text{H}_2\text{O}$ and $\text{Na}_2\text{S} \cdot 9\text{H}_2\text{O}$, the $\text{CoC}_2\text{O}_4 \cdot 2\text{H}_2\text{O}$ and $\text{ZnC}_2\text{O}_4 \cdot 2\text{H}_2\text{O}$ are transferred into the intermediate phase of $\text{Zn}_{0.76}\text{Co}_{0.24}\text{S}@\text{CoSO}_4 \cdot 6\text{H}_2\text{O}$, which can be proved by the XRD spectrum shown in Fig. S1. The XRD spectra of pure ZCS and $\text{ZCS}@CH$ are shown in Fig. 1b. For the $\text{ZCS}@CH$ sample, peaks at 18.8° , 32.2° , 37.6° , 51.1° and 57.6° are indexed to the (001),

(100), (101), (102) and (110) planes of $\text{Co}(\text{OH})_2$ (JCPDS: 45-0031), and the other peaks at 28.6° , 33.1° , 47.6° and 56.5° are corresponding to the (111), (200), (220) and (311) planes of $\text{Zn}_{0.76}\text{Co}_{0.24}\text{S}$ (JCPDS: 47-1656), respectively. These results confirm that the hybrid $\text{ZCS}@CH$ has been successfully synthesized by immersing the intermediate phase of $\text{Zn}_{0.76}\text{Co}_{0.24}\text{S}@CoSO_4$ into the 2 M KOH solution. For comparison, the peaks of pure ZCS sample only show the crystal planes of $\text{Zn}_{0.76}\text{Co}_{0.24}\text{S}$ as shown in Fig. 2b.

Morphology of precursor ($\text{ZnC}_2\text{O}_4@CoC_2O_4$, as shown in the SEM image of Fig. 2c) presents a polyhedral structure, and the surface is smooth. After the hydrothermal reaction in the solution of $\text{Na}_2\text{SO}_4 \cdot 10\text{H}_2\text{O}$ and $\text{Na}_2\text{S} \cdot 9\text{H}_2\text{O}$, the $\text{ZnC}_2\text{O}_4@CoC_2O_4$ precursor has been changed into nanosheets coated nanoparticles of $\text{Zn}_{0.76}\text{Co}_{0.24}\text{S}@CoSO_4 \cdot 6\text{H}_2\text{O}$, indicating the occurrence of recrystallization during the hydrothermal process (see the SEM images in Fig. S2). Fig. 2e shows the formed $\text{ZCS}@CH$ hybrid structure of $\text{Zn}_{0.76}\text{Co}_{0.24}\text{S}$ nanoparticles and $\text{Co}(\text{OH})_2$ hexagonal nanosheets after soaked in the KOH solution. Whereas the pure ZCS is only composed of nanoparticles (Fig. 2d). The estimated average diameter of the $\text{Zn}_{0.76}\text{Co}_{0.24}\text{S}$ nanoparticles is about 20 nm and the thickness and size of $\text{Co}(\text{OH})_2$ nanosheets are about 50 nm and 148 nm (Fig. 2f), respectively.

For the $\text{ZCS}@CH$ hybrid, the $\text{Zn}_{0.76}\text{Co}_{0.24}\text{S}$ nanoparticles are uniformly distributed on $\text{Co}(\text{OH})_2$ nanosheets. Compared with that of the pure ZCS, the $\text{ZCS}@CH$ hybrid structure provides more ion diffusion channels between the active materials and electrolyte, which is favorable for the redox reactions during the charging and discharging processes [27].

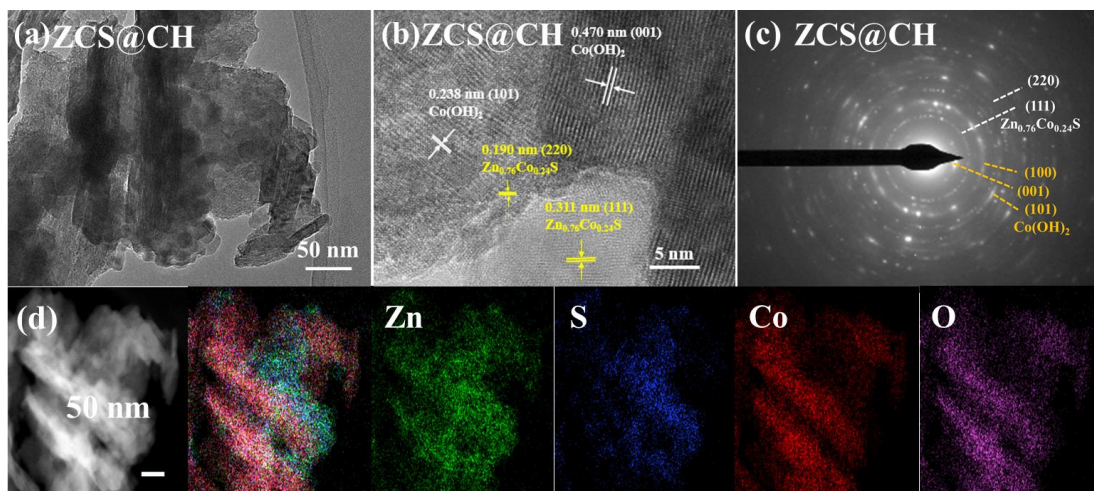


Fig. 3 (a) TEM image of ZCS@CH, (b) HR-TEM image of ZCS@CH, (c) the SAED pattern, and (d) element mapping of ZCS@CH sample.

Fig. 3a shows a TEM image of ZCS@CH, which is well matched with the SEM image shown in Fig. 2e. A high-resolution TEM image of ZCS@CH is shown in Fig. 3b, and the estimated lattice fringes of 0.190 nm and 0.311 nm are corresponding to the (220) and (111) planes of $\text{Zn}_{0.76}\text{Co}_{0.24}\text{S}$, respectively. The other lattice fringes of 0.238 nm and 0.470 nm are corresponding to the (101) and (001) planes of $\text{Co}(\text{OH})_2$. The selected area electron diffraction (SAED) patterns of the ZCS@CH is shown in Fig. 3c, in which the diffraction rings are corresponding to the crystalline facets of the $\text{Zn}_{0.76}\text{Co}_{0.24}\text{S}$ and $\text{Co}(\text{OH})_2$. This clearly reveals the polycrystalline nature of the electrode material.

Fig. 3d shows the element mapping of the ZCS@CH. The elements of Co and O are mainly concentrated on the nanosheets, whereas the elements of Zn and S are concentrated on the nanoparticles. The distribution of elements of Zn, Co, O and S clearly reveals that nanosheets and nanoparticles are evenly distributed inside the sample.

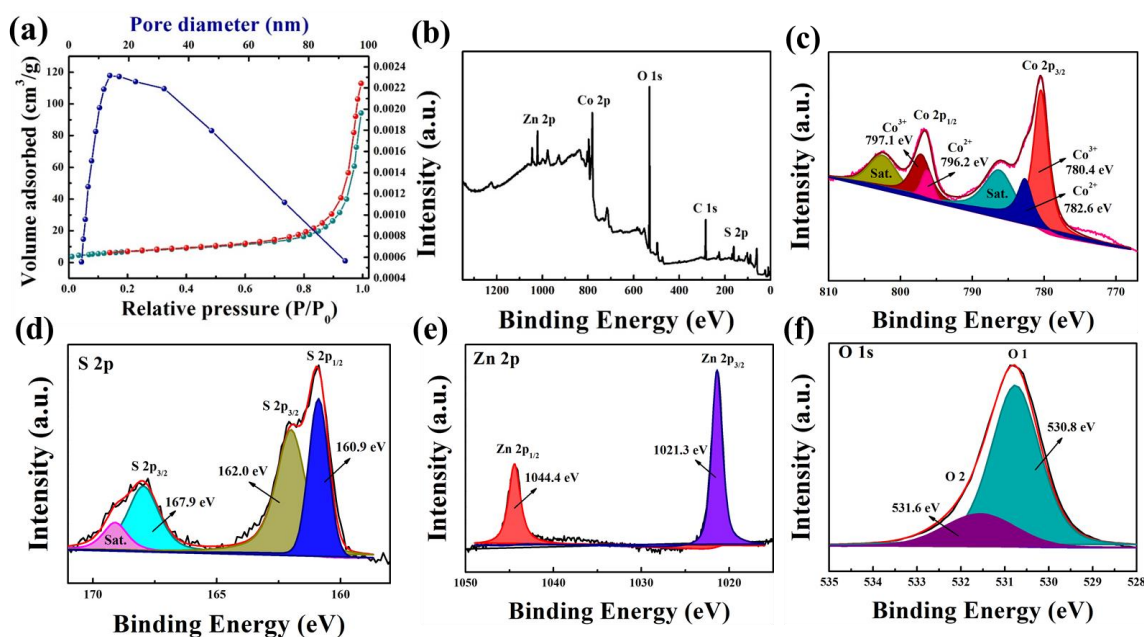


Fig. 4 (a) N_2 adsorption/desorption isotherm and the pore size distributions of ZCS@CH, XPS analysis of ZCS@CH: (b) full spectrum, high resolution of (c) Co 2p, (d) S 2p, (e) Zn 2p and (f) O 1s.

Fig. 4a shows the nitrogen adsorption/desorption isotherm results in the range of 0.0~1.0 P/P_0 . The IV adsorption behavior with a hysteresis loop clearly shows the presence of mesoporous structures in ZCS@CH [28]. Pore volumes and surface areas of the ZCS@CH were calculated using the Barrett-Joyner-Halenda (BJH) and BET method, and the obtained results are $0.159\text{ cm}^3\text{ g}^{-1}$ and $25.0\text{ m}^2\text{ g}^{-1}$, respectively. The nanoparticles and nanosheets form a wide range pore size distribution from 2 nm to 90 nm, with an average size of 15 nm. The porous structures and large specific surface areas of the electrode materials are favorable for the diffusion of electrolyte ions to enhance the faraday reactions [29].

XPS survey spectrum of ZCS@CH is shown in Fig. 4b, revealing the Co, S, Zn, O, C elements in the sample. The element of C is mainly due to the surface adsorption of

contaminates from the air [15, 20]. For the high-resolution Co 2p spectrum in Fig. 4c, the spin-orbits of Co 2p_{3/2} and Co 2p_{1/2} can be separated into two peaks, e.g., Co²⁺ and Co³⁺ [30]. The peaks of 780.4 and 797.1 eV are corresponding to those of the Co³⁺ 2p_{3/2} and Co³⁺ 2p_{1/2}, while the other peaks at 782.6 eV and 796.2 eV are corresponding to those of Co²⁺ 2p_{3/2} and Co²⁺ 2p_{1/2}, respectively [7, 31-33]. Meanwhile, the peaks at 802.4 eV and 786.2 eV are the two satellite peaks of Co²⁺ and Co³⁺ [34], which indicates the co-existence of Co²⁺ and Co³⁺ in the ZCS@CH. The mixed valence states of ZCS@CH, such as Zn_{0.76}Co_{0.24}S with Co²⁺ and Co³⁺, and Co(OH)₂ with Co²⁺, can achieve a high conductivity [35]. The high-resolution spectrum of S 2p is shown in Fig. 4d. The peaks at 162.0 eV and 160.9 eV are corresponding to S 2p_{3/2} and S 2p_{1/2}, respectively. The other peak at 167.9 eV is indexed to the sulfur species at higher oxidation states [19, 36, 37]. Fig. 4e displays the Zn 2p spectrum, which can be well fitted with two peaks at 1044.4 eV and 1021.3 eV, corresponding to Zn 2p_{1/2} and Zn 2p_{3/2} peaks of Zn²⁺, respectively [38]. The O 1s spectrum is shown in Fig. 4f. The peak of O 1s at 530.8 eV represents the lattice oxygen in Co(OH)₂, and the peak at 531.6 eV represents the hydroxyl group on surface [39, 40]. All these XPS results are consistent with those from the XRD analysis and further confirm the formation of the ZCS@CH.

3.2 Electrochemical performance

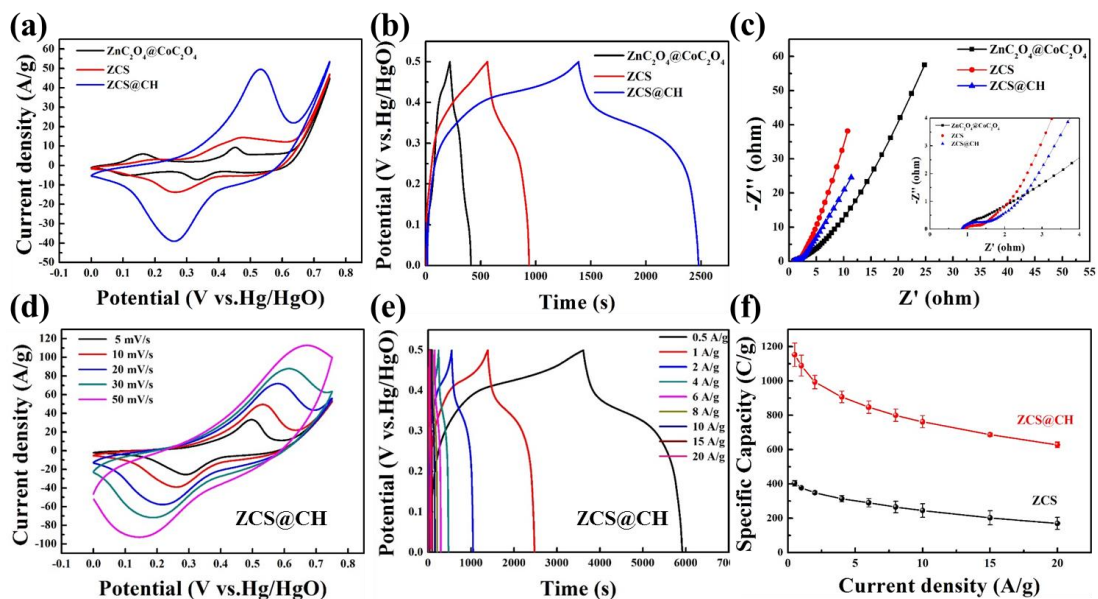
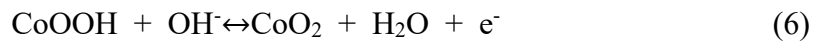
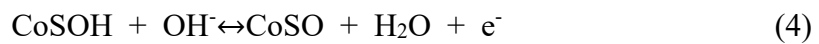


Fig. 5 (a) CV curves of ZnC₂O₄@CoC₂O₄, ZCS and ZCS@CH at a scan rate of 10 mV s⁻¹, (b) GCD curves of ZnC₂O₄@CoC₂O₄, ZCS and ZCS@CH at current density of 1 A g⁻¹, (c) Nyquist plots of the ZnC₂O₄@CoC₂O₄, ZCS and ZCS@CH electrodes, (d) CV curves of ZCS@CH at various scan rates, (e) GCD curves ZCS@CH at various current densities, (f) the specific capacity of ZCS and ZCS@CH at different current densities.

Figs. 5a and 5b show the CV and GCD curves of ZnC₂O₄@CoC₂O₄, ZCS and ZCS@CH electrodes tested using the three-electrode system in the 2 M KOH solution. The closed area and the discharging times of the ZCS@CH electrode are obviously larger than those of the ZCS and ZnC₂O₄@CoC₂O₄, which implies that the ZCS@CH electrode material has the largest specific capacity among these three samples. The Nyquist plots of ZnC₂O₄@CoC₂O₄, ZCS and ZCS@CH electrodes obtained in the frequency range of 0.01~100 kHz are shown in Fig. 5c. The EIS curves consist of a semicircle in the high frequency region and a linear section in the low frequency region, indicating that these three electrode materials are diffusion-controlled battery-type ones

[27]. Based on the high frequency image shown in Fig. 5c inset, the $\text{ZnC}_2\text{O}_4@\text{CoC}_2\text{O}_4$ precursor has a large semicircle and small linear slope compared with those of the other electrodes, which is due to the poor electrical conductivity and low ion transport rates of charged particles [41]. The ZCS@CH electrode has a small equivalent series resistance ($R_s=0.88 \ \Omega$) and a low charge transfer resistance ($R_{ct}= 0.69 \ \Omega$), obtained using the resistance fitting, suggesting that the ZCS@CH has a good conductivity and transport rate of ions [42]. The equivalent circuits of ZCS@CH electrode obtained using a fitting software are shown in Fig. S3 and the results are also listed in Table S1.

Fig. 5d displays the CV curves of ZCS@CH electrode in the potential range of 0 to 0.75 V at different scan rates from 5 mV to 50 mV. These curves have a pair of symmetric redox peaks, which are shifted to positive and negative potentials, respectively, due to the polarization effect [43]. All the CV curves have similar shapes at various scanning rates as shown in Fig. 5d, indicating that ZCS@CH electrode is a diffusion-controlled battery type and has a good reversibility during the following faradaic reactions at the electrode [9, 20, 44-46]:



By fitting the logarithmic relationships between different scanning rates ν (mV s^{-1}) and redox peak current i (A) based on CV curves, the energy storage mechanism of ZCS@CH electrode materials can be investigated using the following equations [47-

49].

$$i = av^b \quad (7)$$

$$\log i = \log a + b \log v \quad (8)$$

where a and b are the adjustable parameters, and the different ranges of b values represent different modes of energy storage. The value of b can be calculated from the linear relationship between $\log i$ and $\log v$. The b value of 1 represents a fully surface-controlled behavior of capacitive-type materials and b value of 0.5 represent a fully diffusion-controlled behavior for battery-type materials [27]. Fig. S4 shows the logarithm relationships between the anodic peak and scan rate of ZCS@CH. The obtained b value is 0.53 for the ZCS@CH, indicating that the diffusion-controlled faradaic reaction is dominant in the charge-discharge processes [50,51].

GCD curves of the ZCS@CH electrode with a potential window of 0~0.5 V at various current densities are shown in Fig. 5e. All the curves display good symmetry patterns, which indicates good coulomb efficiencies of this electrode [52]. There are obvious charge-discharge platforms, indicating the dominant diffusion-control behavior of the electrode, which is consistent with the result of CV analysis. According to the GCD data, the specific capacity values C_s ($C\ g^{-1}$) of ZCS, ZCS@CH and $ZnC_2O_4@CoC_2O_4$ can be obtained based on the Eq. 9 [53]:

$$C_s = \frac{I \times \Delta t}{m} \quad (9)$$

where I (A) is the discharge current, Δt (s) is the discharge time, and m (g) is the mass of the active material. As shown in Fig. 5f, the specific capacity of ZCS@CH electrode is much larger than that of pure ZCS. The C_s values of ZCS@CH electrode are 1152.2,

1089.1, 993.5, 906.8, 847.2, 800.0, 762.0 C g⁻¹ at 0.5, 1, 2, 4, 6, 8, 10 A g⁻¹, respectively.

When the current density is increased from 1 A g⁻¹ to 10 A g⁻¹, the ZCS@CH electrode displays an excellent capacity retention of 70.0%. When the current density is increased to 20 A g⁻¹, the C_s of ZCS@CH electrode can still maintain a value of 628.0 C g⁻¹, meaning its good rate capability. The cycling performance, coulombic and energy efficiencies of ZCS@CH electrode are shown in Fig. S5. At a current density of 20 A g⁻¹, the specific capacity can remain ~73.8% of its the initial value after 5,000 cycles. The corresponding coulombic and energy efficiencies remain ~99.1% and ~64.1%, respectively.

The electrochemical test results of ZnC₂O₄@CoC₂O₄ and ZCS electrodes are shown in Figs. S6 and S7. The ZnC₂O₄@CoC₂O₄ and ZCS electrodes show the capacity values of ~203.1 C g⁻¹ and ~404.2 C g⁻¹ at 0.5 A g⁻¹, respectively. Clearly the results of the ZCS@CH electrode are much better than those of either ZCS or ZnC₂O₄@CoC₂O₄ electrodes. The large specific capacity for the ZCS@CH is mainly attributed to the synergistic effects of Zn_{0.76}Co_{0.24}S nanoparticles and highly conductive Co(OH)₂ nanosheets with large specific surface areas and abundant active sites. Therefore, the ZCS@CH electrode can effectively contact with the electrolyte and facilitate the faradaic reactions, thus achieving good electrochemical properties. Compared with the composite electrode materials (for both Zn_{0.76}Co_{0.24}S, Co(OH)₂) reported in the literature, the ZCS@CH developed in this study shows the highest specific capacity value as listed in Table 1.

Table 1 Summary of capacity properties of related materials in literature.

Materials	Method	Morphology	electrolyte	Capacity
Zn _{0.76} Co _{0.24} S [20]	Hydrothermal	Nanoparticles	2 M KOH	1269.1 F g ⁻¹ at 0.5 A g ⁻¹
Zn _{0.76} Co _{0.24} S@CNTs/GO [35]	Solvothermal	Yolk-shell spheres	6 M KOH	578.6 F g ⁻¹ at 1 A g ⁻¹
CoNi-MOF/carbon fiber [54]	Electrodeposition	Petal-like nanosheets	1 M KOH	1044.0 F g ⁻¹ at 2 A g ⁻¹
Co(OH) ₂ @Ni(OH) ₂ [55]	Electrodeposition	Nanosheets	2 M KOH	355.2 C g ⁻¹ at 1 A g ⁻¹
Co(OH) ₂ /SnO _x /Ni foam [56]	Hydrothermal	Petal-like nanosheets	3 M KOH	806.3 F g ⁻¹ at 1 A g ⁻¹
NiCo ₂ O ₄ @ α -Co(OH) ₂ [57]	Hydrothermal/ electrodeposition	Core-shell nanowires	2 M KOH	1298.0 F g ⁻¹ at 1 A g ⁻¹
Co(OH) ₂ @FeCo ₂ O ₄ [58]	Hydrothermal	Nanoparticles/ nanosheets	6 M KOH	1173.4 F g ⁻¹ at 1 A g ⁻¹
Co ₉ S ₈ @Ni(OH) ₂ [37]	Electrodeposition	Core-shell nanotube	6 M KOH	149.44 mAh g ⁻¹ at 1A g ⁻¹
NiCo ₂ S ₄ @Co(OH) ₂ /Ni [23]	Hydrothermal/ electrodeposition	Core-shell nanotube arrays	2 M KOH	1054.9 F g ⁻¹ at 2 mA cm ⁻²
Zn_{0.76}Co_{0.24}S@Co(OH)₂ (This work)	Hydrothermal	Nanoparticles/ nanosheets	2 M KOH	1152.2 C g⁻¹ at 0.5 A g⁻¹

3.3 Electrochemical properties of hybrid supercapacitor device assembled by ZCS@CH and AC

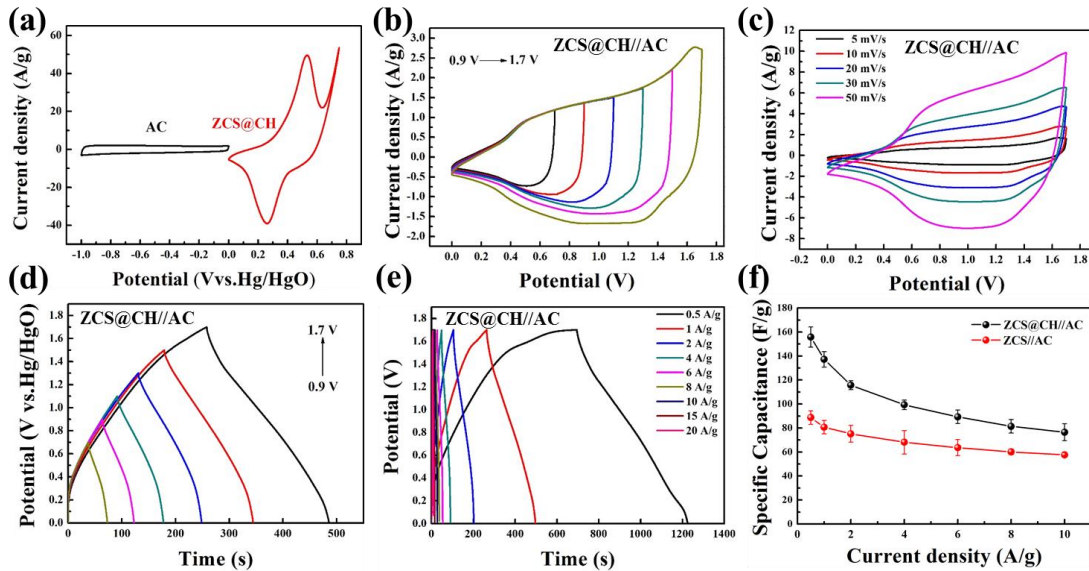


Fig. 6 Electrochemical performance of the as-fabricated ZCS@CH//AC HSC device.

(a) CV curves of ZCS@CH and AC electrode in three-electrode test at a scan rate of 10 mV s⁻¹, (b) CV curves in different potential window at 10 mV s⁻¹, (c) CV curves at

various scan rates, (d) GCD curves in different potential window at a current density of 1 A g^{-1} , (e) GCD curves at different current densities, (f) the specific capacitances of ZCS//AC and ZCS@CH//AC HSCs at various current densities.

Fig. 6a shows the CV curves of ZCS@CH and AC at a scan rate of 10 mV s^{-1} for the HSC device assembled using ZCS@CH (positive electrode) and AC (negative electrode) in 2 M KOH . Fig. 6b shows the CV curves of the HSC obtained at various potential ranges at 10 mV s^{-1} . Results show that the optimal operating voltage of the ZCS@CH//AC HSC is $0\sim 1.7 \text{ V}$, at which the polarization is not observed. Fig. 6c represents the CV curves obtained at different scan rates at a potential window of $0\sim 1.7 \text{ V}$. All the CV curves show a quasi-rectangular shape, indicating that the HSC has a capacitive characteristic [39]. Fig. 6d shows the obtained GCD curves of the HSC tested in different potential windows at a current density of 1 A g^{-1} , and the results show that the stable working potential range of HSC is $0\sim 1.7 \text{ V}$. Fig. 6e shows the GCD curves of the HSC obtained at different current densities, and the specific capacitance C_{HSC} (F g^{-1}) of the HSC can be calculated according to the following Eq. [59]:

$$C_{HSC} = \frac{I \times \Delta t}{M \Delta V} \quad (10)$$

where ΔV (V) is the potential window, Δt (s) is the discharge time. The obtained C_{HSC} values of ZCS@CH//AC HSC based on GCD data are 155.7 F g^{-1} , 137.1 F g^{-1} , 115.6 F g^{-1} , 99.3 F g^{-1} , 89.3 F g^{-1} , 81.4 F g^{-1} , and 76.4 F g^{-1} at $0.5, 1, 2, 4, 6, 8$ and 10 A g^{-1} , respectively. This results are much better than those of the ZCS//AC HSC as shown in Fig. 6f.

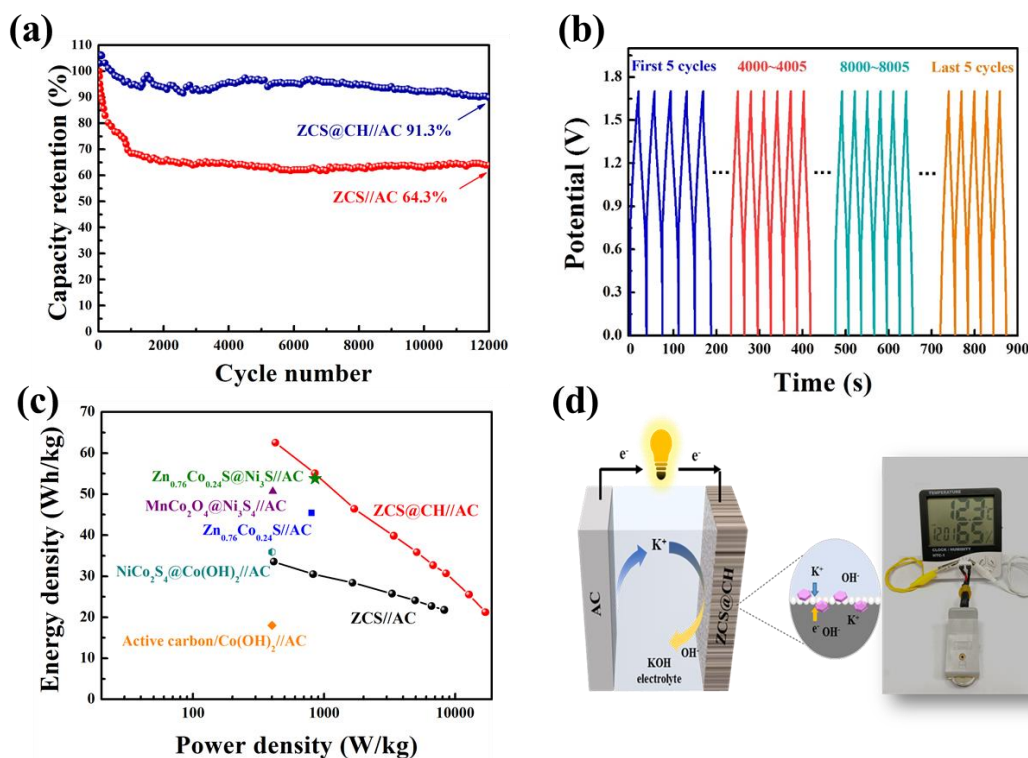


Fig. 7 (a) Cycling performance of ZCS@CH//AC and ZCS//AC HSC at a current density of 8 A g^{-1} , (b) GCD curves of ZCS@CH//AC at different cycles, (c) Ragone plot comparison of ZCS@CH//AC, ZCS//AC and some related asymmetric devices, (d) Schematic illustration and lighted LEDs with ZCS@CH//AC HSC.

The cycling durability of the ZCS@CH//AC and ZCS//AC HSC devices were further characterized at a current density of 8 A g^{-1} , and the obtained results are shown in Fig. 7a. Apparently, the ZCS@CH//AC HSC exhibits a better electrochemical stability than the ZCS//AC HSC. Within the first 100 cycles, the capacitance of ZCS@CH//AC HSC increases because of the activation process of electrode materials [60, 61]. Subsequently, due to structural degradation during the charging and discharging processes, the capacity gradually decreases and eventually remains $\sim 91.3\%$ of its initial value after 12,000 charge-discharge cycles. The corresponding coulombic and energy efficiencies of ZCS@CH//AC remain $\sim 99.8\%$ and $\sim 75.9\%$, respectively (see in Fig. S8). Whereas

the capacitance of the ZCS//AC HSC remains only 64.3% of its initial value after 12,000 cycles. The results clearly demonstrate the better stability of hybrid structures compared with that of each component. Meanwhile, the shapes of GCD curves of ZCS@CH//AC at different cycles (Fig. 7b) do not show apparent changes, indicating its good reversibility and stability. Compared with the other reported HSCs assembled with $\text{Zn}_{0.76}\text{Co}_{0.24}\text{S}$, $\text{Co}(\text{OH})_2$ and the composite electrodes in the literature as listed in Table 2, the ZCS@CH//AC HSC developed in this study show an excellent stability.

Table 2 Summary of the HSC electrochemical properties of this study and the related materials in literature.

HSC device	Cycling stability	Energy density
$\text{Zn}_{0.76}\text{Co}_{0.24}\text{S//AC}$ [20]	91.6% after 5000 cycles	45.4 Wh kg^{-1} at 805.0 W kg^{-1}
$\text{NiCo}_2\text{O}_4@\alpha\text{-Co}(\text{OH})_2\text{//AC}$ [57]	83.0% after 5000 cycles	39.7 Wh kg^{-1} at 387.5 W kg^{-1}
$\text{Co}(\text{OH})_2/\text{SnO}_x/\text{Ni Foam}\text{//AC}$ [56]	64.4% after 2000 cycles	49.7 Wh kg^{-1} at 1599.9 W kg^{-1}
$\text{CoNi-OH-MOF/Carbon Fiber Paper}\text{//AC}$ [54]	94.0% after 5000 cycles	28.5 Wh kg^{-1} at 1500.0 W kg^{-1}
$\text{Co}(\text{OH})_2\text{-MoSe}_2\text{//AC}$ [62]	86.2% after 3000 cycles	30.1 Wh kg^{-1} at 985.7 W kg^{-1}
$\text{Zn}_{0.76}\text{Co}_{0.24}\text{S}@\text{Ni}_3\text{S}_2/\text{NiFoam}\text{//AC}$ [22]	90.3% after 5000 cycles	53.8 Wh kg^{-1} at 853.0 W kg^{-1}
$\text{Co}_9\text{S}_8@\text{Ni}(\text{OH})_2/\text{Carbon Fibers}\text{//AC}$ [37]	97.3% after 5000 cycles	31.3 Wh kg^{-1} at 252.8 W kg^{-1}
$\text{Ni-Co LDH/Co}_9\text{S}_8/\text{Ni Foam}\text{//AC}$ [63]	86.4% after 5000 cycles	50.0 Wh kg^{-1} at 839.0 W kg^{-1}
$\text{NiCo}_2\text{S}_4@\text{Co}(\text{OH})_2/\text{Ni Foam}\text{//AC}$ [23]	70.0% after 5000 cycles	35.8 Wh kg^{-1} at 400.0 W kg^{-1}
$\text{Zn}_{0.76}\text{Co}_{0.24}\text{S}@\text{Co}(\text{OH})_2\text{//AC}$ (This work)	91.3% after 12000 cycles	62.5 Wh kg^{-1} at 425.0 W kg^{-1}

Energy density E (Wh kg^{-1}) and power density P (W kg^{-1}) of the HSC can be obtained using the following Equations:

$$E = \frac{C_{\text{HSC}} \times (\Delta V)^2}{2 \times 3.6} \quad (11)$$

$$P = \frac{E \times 3600}{\Delta t} \quad (12)$$

where C_{HSC} ($F\ g^{-1}$) is the specific capacitance of HSC. The ZCS@CH//AC HSC achieves an energy density of $62.5\ Wh\ kg^{-1}$ at a power density of $425.0\ W\ kg^{-1}$. Its energy density keeps a value of $21.3\ Wh\ kg^{-1}$ at a power density of $17.0\ kW\ kg^{-1}$. Fig. 7c shows the Ragone plots of ZCS@CH//AC, ZCS//AC HSCs and other similar devices. Based on this figure, the energy density of ZCS@CH//AC HSC is superior to most of composite electrodes reported in literature. These include $Zn_{0.76}Co_{0.24}S//AC$ ($45.5\ Wh\ kg^{-1}$ at $805.0\ W\ kg^{-1}$) [20], $Zn_{0.76}Co_{0.24}S@Ni_3S_2//AC$ ($53.8\ Wh\ kg^{-1}$ at $853.0\ W\ kg^{-1}$) [22], $MnCo_2O_4/Ni_3S_4//AC$ ($50.7\ Wh\ kg^{-1}$ at $405.8\ W\ kg^{-1}$) [49], $NiCo_2S_4@Co(OH)_2//AC$ ($35.9\ Wh\ kg^{-1}$ at $400.0\ W\ kg^{-1}$) [23] and active carbon/ $Co(OH)_2//AC$ ($18.0\ Wh\ kg^{-1}$ at $400.0\ W\ kg^{-1}$) [16].

Fig. 7d shows a schematic illustration of HSC device which was assembled by using ZCS@CH//AC. To verify the practical applications, three as-prepared HSCs devices were connected in series and used to power the light-emitting diodes (LEDs). The LEDs can be switched on under a short charge, showing a great potential for practical application of hybrid ZCS@CH//AC devices. Therefore, the ZCS@CH is an excellent electrode material for supercapacitors.

4 Conclusions

The hybrid composites of ZCS nanoparticles and $Co(OH)_2$ nanosheets were successfully synthesized via a two-step hydrothermal. Synergetic effects of the hybrid structure can achieve excellent electrochemical properties due to the various active sites and small pore size. The specific capacity of ZCS@CH was $1089.1\ C\ g^{-1}$ at the current

density of 1 A g^{-1} and remained 70.0% of its original value at 10 A g^{-1} . Meanwhile, the ZCS@CH//AC HSC achieved a high energy density 62.5 Wh kg^{-1} at the power density of 425.0 W kg^{-1} , with an outstanding long-term cycling stability (91.3% after 12,000 cycles). This work proposes a new synthetic strategy for hybrid nanostructures and the ZCS@CH has a promising application in energy storage.

Acknowledgements

This work is supported by the International Exchange Grant (IEC/NSFC/201078) through Royal Society UK and National Natural Science Foundation of China.

Reference

- [1] Q. Zhu, D. Zhao, M. Cheng, J. Zhou, K.A. Owusu, L. Mai, Y. Yu, A new view of supercapacitors: Integrated supercapacitors, *Adv. Energy Mater.* 9 (2019) 1901081.
- [2] Z. Yu, B. Duong, D. Abbitt, J. Thomas, Highly ordered MnO_2 nanopillars for enhanced supercapacitor performance, *Adv. Mater.* 25 (2013) 3302-3306.
- [3] F. Hekmat, M. Shahi, S. Shahrokhia, Direct fabrication of phosphorus-doped nickel sulfide and eco-friendly biomass-derived humic acid as efficient electrodes for energy storage applications, *Sustain. Energ. Fuels* 5 (2021) 4869-4881.
- [4] G. Lee, J. Jang, High-performance hybrid supercapacitors based on novel $\text{Co}_3\text{O}_4/\text{Co}(\text{OH})_2$ hybrids synthesized with various-sized metal-organic framework templates, *J. Power Sources* 423 (2019) 115-124.
- [5] H. Li, Z. Li, Z. Wu, M. Sun, S. Han, C. Cai, W. Shen, Y. Fu, Nanocomposites of cobalt sulfide embedded carbon nanotubes with enhanced supercapacitor performance,

J. Electrochem. Soc. 166 (6) (2019) A1031-A1037.

[6] J. Xie, P. Yang, Y. Wang, T. Qi, Y. Lei, C.M. Li, Puzzles and confusions in supercapacitor and battery: Theory and solutions, J. Power Sources 401 (2018) 213-223.

[7] B. Zhao, L. Zhang, Q. Zhang, D. Chen, Y. Cheng, X. Deng, Y. Chen, R. Murphy, X. Xiong, B. Song, C.P. Wong, M.S. Wang, M. Liu, Rational design of nickel Hydroxide - based nanocrystals on graphene for ultrafast energy storage, Adv. Energy Mater. 8 (2017) 1702247.

[8] Y. Zhou, Z. Jia, Y. Shen, L. Wei, S. Zhao, Y. Han, P. Chen, C. Xu, X. Cui, J. Sun, X. Ouyang, X. Wang, J. Zhu, S. Pan, Y. Fu, Ingenious construction of hierarchical spherical nanostructures by in-situ confining Ni-Co-Mn hydroxide nanosheets inside/outside hollow carbon nanospheres for high-performance hybrid supercapacitors, J. Energy Storage 36 (2021) 102380.

[9] W. Gong, M. Wang, Y. An, J. Wang, L. Zhou, Y. Xia, C. Wang, K. Dong, C. Pan, R. Zhou, Rational design and synthesis of hydrotalcite-like α -Co(OH)₂ nanoflakes for extrinsic pseudocapacitive electrodes with superb cycling stability, J. Energy Storage 38 (2021) 102579.

[10] J. Li, H. Hao, J. Wang, W. Li, W. Shen, Hydrogels that couple nitrogen-enriched graphene with Ni(OH)₂ nanosheets for high-performance asymmetric supercapacitors, J. Alloy. Compd. 782 (2019) 516-524.

[11] D. Zhu, M. Yan, R. Chen, Q. Liu, J. Liu, J. Yu, H. Zhang, M. Zhang, P. Liu, J. Li, J. Wang, 3D Cu(OH)₂ nanowires/carbon cloth for flexible supercapacitors with

outstanding cycle stability, Chem. Eng. J. 371 (2019) 348-355.

[12] Y. Du, G. Li, L. Ye, C. Che, X. Yang, L. Zhao, Sandwich-like Ni-Zn hydroxide nanosheets vertically aligned on reduced graphene oxide via MOF templates towards boosting supercapacitive performance, Chem. Eng. J. 417 (2021) 129189.

[13] S. Wang, Z. Zhu, P. Li, C. Zhao, C. Zhao, H. Xia, In situ conversion of sub-4 nm $\text{Co}(\text{OH})_2$ nanosheet arrays from phytic acid-derived $\text{Co}_3(\text{HPO}_4)_2(\text{OH})_2$ for superior high loading supercapacitors, J. Mater. Chem. A 6 (2018) 20015-20024.

[14] Q. Yang, Q. Wang, Y. Long, F. Wang, L. Wu, J. Pan, J. Han, Y. Lei, W. Shi, S. Song, In situ formation of Co_9S_8 quantum dots in MOF-derived ternary metal layered double hydroxide nanoarrays for high-performance hybrid supercapacitors, Adv. Energy Mater. 10 (2020) 1903193.

[15] T. Xu, G. Li, L. Zhao, Ni-Co-S/ $\text{Co}(\text{OH})_2$ nanocomposite for high energy density all-solid-state asymmetric supercapacitors, Chem. Eng. J. 336 (2018) 602-611.

[16] C. Xu, Y. Chen, Y. Ma, J. Huang, J. Zhao, H. Xu, Waste activated carbon transformed to electrode of supercapacitor through combining with $\text{Co}(\text{OH})_2$, Electrochim. Acta 367 (2021) 137475.

[17] M. Xu, H. Guo, R. Xue, M. Wang, N. Wu, X. Wang, J. Zhang, T. Zhang, W. Yang, Sandwich-like $\text{GO}@\text{Co}(\text{OH})_2/\text{PANI}$ derived from MOFs as high-performance electrode for supercapacitors, J. Alloy. Compd. 863 (2021) 157699.

[18] A.M. Elshahawy, X. Li, H. Zhang, Y. Hu, K.H. Ho, C. Guan, J. Wang, Controllable MnCo_2S_4 nanostructures for high performance hybrid supercapacitors, J. Mater. Chem. A 5 (2017) 7494-7506.

- [19] S. Vijayakumar, G. Dhakal, S.H. Kim, J. Lee, Y.R. Lee, J.J. Shim, Facile synthesis of Zn-Co-S nanostrip cluster arrays on Ni foam for high-performance hybrid supercapacitors, *Nanomaterials-Basel* 11 (2021) 3209.
- [20] H. Li, Z. Li, M. Sun, Z. Wu, W. Shen, Y.Q. Fu, Zinc cobalt sulfide nanoparticles as high performance electrode material for asymmetric supercapacitor, *Electrochim. Acta* 319 (2019) 716-726.
- [21] Y. Zhang, N. Cao, S. Szunerits, A. Addad, P. Roussel, R. Boukherroub, Fabrication of ZnCoS nanomaterial for high energy flexible asymmetric supercapacitors, *Chem. Eng. J.* 374 (2019) 347-358.
- [22] Y. Lv, A. Liu, Z. Shi, H. Che, J. Mu, Z. Guo, X. Zhang, Construction of hierarchical zinc cobalt sulfide@nickel sulfide core-shell nanosheet arrays for high-performance asymmetric solid-state supercapacitors, *Chem. Eng. J.* 349 (2018) 397-407.
- [23] R. Li, S. Wang, Z. Huang, F. Lu, T. He, NiCo₂S₄@Co(OH)₂ core-shell nanotube arrays in situ grown on Ni foam for high performances asymmetric supercapacitors, *J. Power Sources* 312 (2016) 156-164.
- [24] X. Guan, M. Huang, L. Yang, G. Wang, X. Guan, Facial design and synthesis of CoS_x/Ni-Co LDH nanocages with rhombic dodecahedral structure for high-performance asymmetric supercapacitors, *Chem. Eng. J.* 372 (2019) 151-162.
- [25] B. Wu, F. Zhang, Z. Nie, H. Qian, P. Liu, H. He, J. Wu, Z. Chen, S. Chen, A high-performance battery-like supercapacitor electrode with a continuous NiTe network skeleton running throughout Co(OH)₂/Co₉S₈ nanohybrid, *Electrochim. Acta* 365 (2021) 137325.

- [26] M. Sun, Q. Fang, Z. Li, C. Cai, H. Li, B. Cao, W. Shen, T.X. Liu, Y. Fu, Co-precipitation synthesis of CuCo_2O_4 nanoparticles for supercapacitor electrodes with large specific capacity and high rate capability, *Electrochim. Acta* 397 (2021) 139306.
- [27] C. Ren, X. Jia, W. Zhang, D. Hou, Z. Xia, D. Huang, J. Hu, S. Chen, S. Gao, Hierarchical porous integrated $\text{Co}_{1-x}\text{S}/\text{CoFe}_2\text{O}_4@\text{rGO}$ nanoflowers fabricated via temperature-controlled in situ calcining sulfurization of multivariate $\text{CoFe-MOF-74}@\text{rGO}$ for high-performance supercapacitor, *Adv. Funct. Mater.* 30 (2020) 2004519.
- [28] F. Hekmat, H. Hosseini, S. Shahrokhian, H.E. Unalan, Hybrid energy storage device from binder-free zinc-cobalt sulfide decorated biomass-derived carbon microspheres and pyrolyzed polyaniline nanotube-iron oxide, *Energy Storage Mater.* 25 (2020) 621-635.
- [29] Q. Fang, M. Sun, X. Ren, B. Cao, W. Shen, Z. Li, Y. Fu, Ultrafine Mn_3O_4 nanowires synthesized by colloidal method as electrode materials for supercapacitors with a wide voltage range, *J. Energy Storage* 44 (2021) 103260.
- [30] C. Li, J. Balamurugan, N.H. Kim, J.H. Lee, Hierarchical Zn-Co-S nanowires as advanced electrodes for all solid state asymmetric supercapacitors, *Adv. Energy Mater.* 8 (2018) 1702014.
- [31] M. Shahi, F. Hekmat, S. Shahrokhian, Hybrid supercapacitors constructed from double-shelled cobalt-zinc sulfide/copper oxide nanoarrays and ferrous sulfide/graphene oxide nanostructures, *J. colloid interf. Sci.* (2020) 750-763.
- [32] Y.H. Zhao, H.X. Dong, X.Y. He, J. Yu, R.R. Chen, Q. Liu, J.Y. Liu, H.S. Zhang, R.M. Li, J. Wang, Design of 2D mesoporous Zn/Co-based metal-organic frameworks

as a flexible electrode for energy storage and conversion, *J. Power Sources* 438 (2019) 227057.

[33] J.A. Syed, J. Ma, B. Zhu, S. Tang, X. Meng, Hierarchical multicomponent electrode with interlaced Ni(OH)₂ nanoflakes wrapped zinc cobalt sulfide nanotube arrays for sustainable high-performance supercapacitors, *Adv. Energy Mater.* 7 (2017) 1701228.

[34] H. Chen, M.Q. Wang, Y. Yu, H. Liu, S.Y. Lu, S.J. Bao, M. Xu, Assembling hollow cobalt sulfide nanocages array on graphene-like manganese dioxide nanosheets for superior electrochemical capacitors, *ACS Appl. Mater. Interf.* 9 (2017) 35040-35047.

[35] X. Yu, W. Zhang, L. Liu, Y. Fautrelle, X. Lu, X. Li, High magnetic field-engineered Bunched Zn-Co-S yolk-shell balls intercalated within S, N codoped CNT/Graphene films for free-standing supercapacitors, *ACS Appl. Mater. Interf.* 12 (2020) 33690-33701.

[36] J.X. Feng, J.Q. Wu, Y.X. Tong, G.R. Li, Efficient hydrogen evolution on Cu nanodots-decorated Ni₃S₂ nanotubes by optimizing atomic hydrogen adsorption and desorption, *J. Am. Chem. Soc.* 140 (2018) 610-617.

[37] F. Zhu, M. Yan, Y. Liu, H. Shen, Y. Lei, W. Shi, Hexagonal prism-like hierarchical Co₉S₈@Ni(OH)₂ core-shell nanotubes on carbon fibers for high-performance asymmetric supercapacitors, *J. Mater. Chem. A* 5 (2017) 22782-22789.

[38] H. Wu, X. Zhang, J. Xue, H. Zhang, L. Yang, S. Li, Engineering active sites on hierarchical ZnNi layered double hydroxide architectures with rich Zn vacancies boosting battery-type supercapacitor performances, *Electrochim. Acta* 374 (2021)

137932.

[39] M. Jana, P. Sivakumar, M. Kota, M.G. Jung, H.S. Park, Phase- and interlayer spacing-controlled cobalt hydroxides for high performance asymmetric supercapacitor applications, *J. Power Sources* 422 (2019) 9-17.

[40] X. Sun, X. Sun, S. Zhou, G. Luo, R. Liu, S. Li, A. Li, X. Zhu, Designed construction of hierarchical $\text{CuCo}_2\text{S}_4@\text{Co}(\text{OH})_2$ core-shell nanoarrays as electrode materials for high-performance supercapacitors, *ChemistrySelect* 4 (2019) 7751-7758.

[41] M. Kandasamy, S. Sahoo, S.K. Nayak, B. Chakraborty, C.S. Rout, Recent advances in engineered metal oxide nanostructures for supercapacitor applications: experimental and theoretical aspects, *J. Mater. Chem. A* 9 (2021) 17643-17700.

[42] Y. He, L. Xie, S. Ding, Y. Long, X. Zhou, Q. Hu, D. Lin, Core-shell nanostructured $\text{Zn-Co-O}@\text{CoS}$ arrays for high-performance hybrid supercapacitors, *Dalton T.* 50 (2021) 4923-4931.

[43] H. Li, Z. Li, Z. Wu, M. Sun, S. Han, C. Cai, W. Shen, X. Liu, Y. Fu, Enhanced electrochemical performance of CuCo_2S_4 /carbon nanotubes composite as electrode material for supercapacitors, *J. Colloid Interf. Sci* 549 (2019) 105-113.

[44] M. Sun, Z. Li, H. Li, Z. Wu, W. Shen, Y.Q. Fu, Mesoporous Zr-doped CeO_2 nanostructures as superior supercapacitor electrode with significantly enhanced specific capacity and excellent cycling stability, *Electrochim. Acta* 331 (2020) 135366.

[45] Q. Deng, Z. Tian, X. Wang, Z. Yang, Y. Wu, Zn-Co sulfide microflowers anchored on three-dimensional graphene: a high-capacitance and long-cycle-life electrode for asymmetric supercapacitors, *Chem-Eur. J.* 26 (2020) 650-658.

- [46] X. Zhang, G. Qu, Z. Wang, G. Xiang, S. Hao, X. Wang, X. Xu, W. Ma, G. Zhao, Hollow polyhedron structure of amorphous Ni-Co-S/Co(OH)₂ for high performance supercapacitors, *Chinese Chem. Lett.* 32 (2021) 2453-2458.
- [47] Y. Zhou, Z. Jia, S. Zhao, Y. Wang, T. Guo, L. Wei, X. Cui, X. Ouoyang, X. Wang, J. Zhu, J. Sun, S. Pan, Construction of triple-shelled hollow nanostructure by confining amorphous Ni-Co-S/crystalline MnS on/in hollow carbon nanospheres for all-solid-state hybrid supercapacitors, *Chem. Eng. J.* 416 (2021) 129500.
- [48] G. Zhou, M.C. Li, C. Liu, Q. Wu, C. Mei, 3D Printed Ti₃C₂T_x MXene/cellulose nanofiber architectures for solid-state supercapacitors: ink rheology, 3D printability, and electrochemical performance, *Adv. Funct. Mater.* (2021) 2109593.
- [49] Q. Fang, M. Sun, X. Ren, Y. Sun, Y. Yan, Z. Gan, J. Huang, B. Cao, W. Shen, Z. Li, Y. Fu, MnCo₂O₄/Ni₃S₄ nanocomposite for hybrid supercapacitor with superior energy density and long-term cycling stability, *J. Colloid Interf. Sci* 611 (2021) 503-512.
- [50] M. Shahi, F. Hekmat, S. Shahrokhia, 3D flower-like nickel cobalt sulfide directly decorated grassy nickel sulfide and encapsulated iron in carbon sphere hosts as hybrid energy storage device, *Appl. Surf. Sci.* 558 (2021) 149869.
- [51] S. Abbasi, F. Hekmat, S. Shahrokhian, Beyond hierarchical mixed nickel-cobalt hydroxide and ferric oxide formation onto the green carbons for energy storage applications, *J. Colloid Interf. Sci.* 593 (2021) 182–195.
- [52] J. Zhao, Z. Li, X. Yuan, T. Shen, L. Lin, M. Zhang, A. Meng, Q. Li, Novel core-shell multi-dimensional hybrid nanoarchitectures consisting of Co(OH)₂

nanoparticles/Ni₃S₂ nanosheets grown on SiC nanowire networks for high-performance asymmetric supercapacitors, *Chem. Eng. J.* 357 (2019) 21-32.

[53] Q. Yang, Y. Liu, L. Xiao, M. Yan, H. Bai, F. Zhu, Y. Lei, W. Shi, Self-templated transformation of MOFs into layered double hydroxide nanoarrays with selectively formed Co₉S₈ for high-performance asymmetric supercapacitors, *Chem. Eng. J.* 354 (2018) 716-726.

[54] T. Deng, Y. Lu, W. Zhang, M. Sui, X. Shi, D. Wang, W. Zheng, Inverted design for high-performance supercapacitor via Co(OH)₂-derived highly oriented MOF electrodes, *Adv. Energy Mater.* 8 (2018) 1702294.

[55] A. Sharifi, M. Arvand, S. Daneshvar, A novel flexible wire-shaped supercapacitor with enhanced electrochemical performance based on hierarchical Co(OH)₂@Ni(OH)₂ decorated porous dendritic Ni film/Ni wire, *J. Alloy. Compd.* 856 (2021) 158101.

[56] Y. Li, J. Ma, S. Yang, L. Cui, H. Lu, One-step synthesis of Co(OH)₂/SnO₂/C hybrid nanosheets for asymmetric solid-state supercapacitors, *J. Alloy. Compd.* 881 (2021) 160508.

[57] W.D. Wang, P.P. Zhang, S.Q. Gao, B.Q. Wang, X.C. Wang, M. Li, F. Liu, J.P. Cheng, Core-shell nanowires of NiCo₂O₄@α-Co(OH)₂ on Ni foam with enhanced performances for supercapacitors, *J. Colloid Interf. Sci* 579 (2020) 71-81.

[58] Z. Wang, P. Hong, S. Peng, T. Zou, Y. Yang, X. Xing, Z. Wang, R. Zhao, Z. Yan, Y. Wang, Co(OH)₂@FeCo₂O₄ as electrode material for high performance faradaic supercapacitor application, *Electrochim. Acta* 299 (2019) 312-319.

[59] C. Shen, X. Guan, Y. Tang, X. Zhao, Y. Zuo, A zinc-cobalt-nickel heterostructure

synthesized by ultrasonic pulse electrodeposition as a cathode for high performance supercapacitors, *J. Electroanalytical Chem.* 902 (2021) 115793.

[60] F. Chen, H. Wang, S. Ji, V. Linkov, R. Wang, Core-shell structured $\text{Ni}_3\text{S}_2@\text{Co}(\text{OH})_2$ nano-wires grown on Ni foam as binder-free electrode for asymmetric supercapacitors, *Chem. Eng. J.* 345 (2018) 48-57.

[61] N. Xin, Y. Liu, H. Niu, H. Bai, W. Shi, In-situ construction of metal organic frameworks derived Co/Zn-S sandwiched graphene film as free-standing electrodes for ultra-high energy density supercapacitors, *J. Power Sources* 451 (2020) 227772.

[62] A. Alam, G. Saeed, S. Lim, One-step synthesis of 2D-2D $\text{Co}(\text{OH})_2\text{-MoSe}_2$ hybrid nanosheets as an efficient electrode material for high-performance asymmetric supercapacitor, *J. Electroanalytical Chem.* 879 (2020) 114775.

[63] H. Jia, Z. Wang, X. Zheng, J. Lin, H. Liang, Y. Cai, J. Qi, J. Cao, J. Feng, W. Fei, Interlaced Ni-Co LDH nanosheets wrapped Co_9S_8 nanotube with hierarchical structure toward high performance supercapacitors, *Chem. Eng. J.* 351 (2018) 348-355.